Author/s:
Stemp, HG;Asaad, S;Blankenstein, MRV;Vaartjes, A;Johnson, MAI;Mądzik, MT;Heskes, AJA;Firgau, HR;Su, RY;Yang, CH;Laucht, A;Ostrove, CI;Rudinger, KM;Young, K;Blume-Kohout, R;Hudson, FE;Dzurak, AS;Itoh, KM;Jakob, AM;Johnson, BC;Jamieson, DN;Morello, A

Title:
Tomography of entangling two-qubit logic operations in exchange-coupled donor electron spin qubits

Date:
2024-12-01

Citation:
Stemp, H. G., Asaad, S., Blankenstein, M. R. V., Vaartjes, A., Johnson, M. A. I., Mądzik, M. T., Heskes, A. J. A., Firgau, H. R., Su, R. Y., Yang, C. H., Laucht, A., Ostrove, C. I., Rudinger, K. M., Young, K., Blume-Kohout, R., Hudson, F. E., Dzurak, A. S., Itoh, K. M., Jakob, A. M. ,... Morello, A. (2024). Tomography of entangling two-qubit logic operations in exchange-coupled donor electron spin qubits. Nature Communications, 15 (1), https://doi.org/10.1038/s41467-024-52795-4.

Persistent Link:
https://hdl.handle.net/11343/358785

nature communications

Article

https://doi.org/10.1038/s41467-024-52795-4

Tomography of entangling two-qubit logic operations in exchange-coupled donor electron spin qubits

Received: 5 April 2024

Accepted: 18 September 2024

Published online: 28 September 2024

Check for updates

Holly G. Stemp[1,2], Serwan Asaad[1,2,8], Mark R. van Blankenstein[1,2], Arjen Vaartjes[1,2], Mark A. I. Johnson[1,2,9], Mateusz T. Mądzik[1,2,10], Amber J. A. Heskes[1,2,11], Hannes R. Firgau[1,2], Rocky Y. Su[1], Chih Hwan Yang[1,3], Arne Laucht[1,3], Corey I. Ostrove[4], Kenneth M. Rudinger[4], Kevin Young[4], Robin Blume-Kohout[4], Fay E. Hudson[1,3], Andrew S. Dzurak[1,3], Kohei M. Itoh[5], Alexander M. Jakob[2,6], Brett C. Johnson[7], David N. Jamieson[2,6] & Andrea Morello[1,2]

Scalable quantum processors require high-fidelity universal quantum logic operations in a manufacturable physical platform. Donors in silicon provide atomic size, excellent quantum coherence and compatibility with standard semiconductor processing, but no entanglement between donor-bound electron spins has been demonstrated to date. Here we present the experimental demonstration and tomography of universal one- and two-qubit gates in a system of two weakly exchange-coupled electrons, bound to single phosphorus donors introduced in silicon by ion implantation. We observe that the exchange interaction has no effect on the qubit coherence. We quantify the fidelity of the quantum operations using gate set tomography (GST), and we use the universal gate set to create entangled Bell states of the electrons spins, with fidelity 91.3 ± 3.0%, and concurrence 0.87 ± 0.05. These results form the necessary basis for scaling up donor-based quantum computers.

The exchange interaction is a fundamental form of coupling between electron spins. It stems from the Pauli exclusion principle, and its amplitude J depends on the overlap between the wave functions of the electrons[1]. In the context of spin-based quantum information processing, the exchange interaction features prominently as a natural method to enable entangling operations between electron spins[2]. For example, preparing two spins $S=1/2$ in opposite states, $|\uparrow\downarrow\rangle$ and switching on the interaction for a time $\pi/2J$ results in the entangled state $(|\uparrow\downarrow\rangle - i|\downarrow\uparrow\rangle)/\sqrt{2}$. In early experiments on electron spin qubits in quantum dots, J was controlled by detuning the two electrons' potentials with respect to each other[3–5]. Progress in device fabrication has allowed the reliable placement of thin gates between pairs of dots, through which J was varied over many orders of magnitude by controlling the height of the tunnel barrier between the dots[6,7]. This method also reduces the sensitivity to charge noise[8,9].

The situation is more complicated in donor-based spin qubits[10]. Encoding quantum information in the nuclear spin of donor atoms in silicon was one of the earliest proposals for solid-state quantum computers[11]. This vision has been corroborated by the experimental demonstration of exceptionally long spin coherence times, exceeding

[1]School of Electrical Engineering and Telecommunications, UNSW Sydney, Sydney, NSW 2052, Australia. [2]ARC Centre of Excellence for Quantum Computation and Communication Technology, Melbourne, VIC, Australia. [3]Diraq Pty. Ltd., Sydney, NSW, Australia. [4]Quantum Performance Laboratory, Sandia National Laboratories, Albuquerque, NM 87185, Livermore, CA 94550, USA. [5]School of Fundamental Science and Technology, Keio University, Kohoku-ku, Yokohama, Japan. [6]School of Physics, University of Melbourne, Melbourne, VIC 3010, Australia. [7]School of Science, RMIT University, Melbourne, VIC 3000, Australia. [8]Present address: Quantum Machines, Copenhagen, Denmark. [9]Present address: Quantum Motion, London, UK. [10]Present address: Intel Corporation Hillsboro, Hillsboro, OR, USA. [11]Present address: University of Twente, Enschede, The Netherlands. e-mail: a.morello@unsw.edu.au

30 s[12], and one- and two-qubit gate fidelities above 99%[13,14]. The Coulomb potential of a donor also naturally binds an electron, which is itself an excellent qubit, with demonstrated single-qubit gate fidelity up to 99.98%[15]. However, electron two-qubit logic gates based on exchange face the challenge that J is both oscillating and exponentially dependent on inter-donor distance[16–18]. The useful range of the exchange is only ~10–20 nm, making it difficult to fabricate and align metallic gates to control the tunnel barrier between the donors. Therefore, the only example of exchange control in donor systems to date was achieved by detuning the electrochemical potentials of a pair of multi-donor quantum dots, resulting in gate-controlled SWAP oscillations[19]. Since the donor-bound electrons were not operated as qubits, it was not possible to benchmark the fidelity of such operations, nor to demonstrate spin entanglement. Even in quantum computer architectures focusing on donor nuclear spins as the information carriers, electron exchange is likely to be a crucial ingredient for scale-up, since nuclear spins do not naturally interact with each other with sufficient strength.

Here we present the first experimental demonstration of exchange-based, entangling two-qubit logic gates between electrons bound to individual ^{31}P donors in silicon. This is obtained by implementing a scheme exploiting a fixed J, weaker than the electron-nuclear hyperfine interaction, A[20]. In this regime, preparing the two ^{31}P nuclei in an opposite state detunes the two electrons by $A \gg J$ and renders each electron's resonance frequency dependent on the state of the other. The native two-qubit operation is a CROT gate (equivalent to a CNOT gate, up to single-qubit rotations), implemented by electron spin resonance[21]. This setup is formally equivalent to that of experiments in gate-defined double quantum dots operating in the regime $J < \Delta E_z$, where ΔE_z is a Zeeman energy difference between the two-electron spins, caused either by a magnetic field gradient[22,23] or by a difference in g-factor across the two dots[24].

Since the precise value of J is irrelevant, provided it is $\ll A$ and larger than the resonance linewidth, this scheme is relatively insensitive to uncertainties in the precise location of the donors. It is thus well suited to ion-implanted donor spins[10,25–27], which retain compatibility with standard metal-oxide-semiconductor manufacturing processes[28]. Both electron spins are operated coherently as individual qubits[29] and read out in single-shot, either directly[30] or via quantum logic[31,32]. This allows us to perform accurate tomography of the one- and two-qubit gate operations, and to show that the weak-J regime does not affect the coherence of the individual spins.

Results

Operation of the two-electron processor

The two-qubit processor consists of electron spins, Q1 and Q2, each with spin $S = 1/2$ and basis states $|\downarrow\rangle$, $|\uparrow\rangle$, bound to ^{31}P donor nuclei with spin I=1/2 and basis states $|\Downarrow\rangle$, $|\Uparrow\rangle$ (Fig. 1a). Denoting with $\mathbf{S_{1,2}}$, $\mathbf{I_{1,2}}$ the vector spin operators for each electron and nucleus, and $A_{1,2}$ the electron-nuclear hyperfine couplings of each atom, the Hamiltonian of the system (in frequency units) is:

$$\begin{aligned} H = &(\mu_B/h)B_0(g_1 S_{z1} + g_2 S_{z2}) \\ &+ \gamma_n B_0(I_{z1} + I_{z2}) \\ &+ A_1 \mathbf{S_1}\cdot\mathbf{I_1} + A_2 \mathbf{S_2}\cdot\mathbf{I_2} \\ &+ J(\mathbf{S_1}\cdot\mathbf{S_2}), \end{aligned} \tag{1}$$

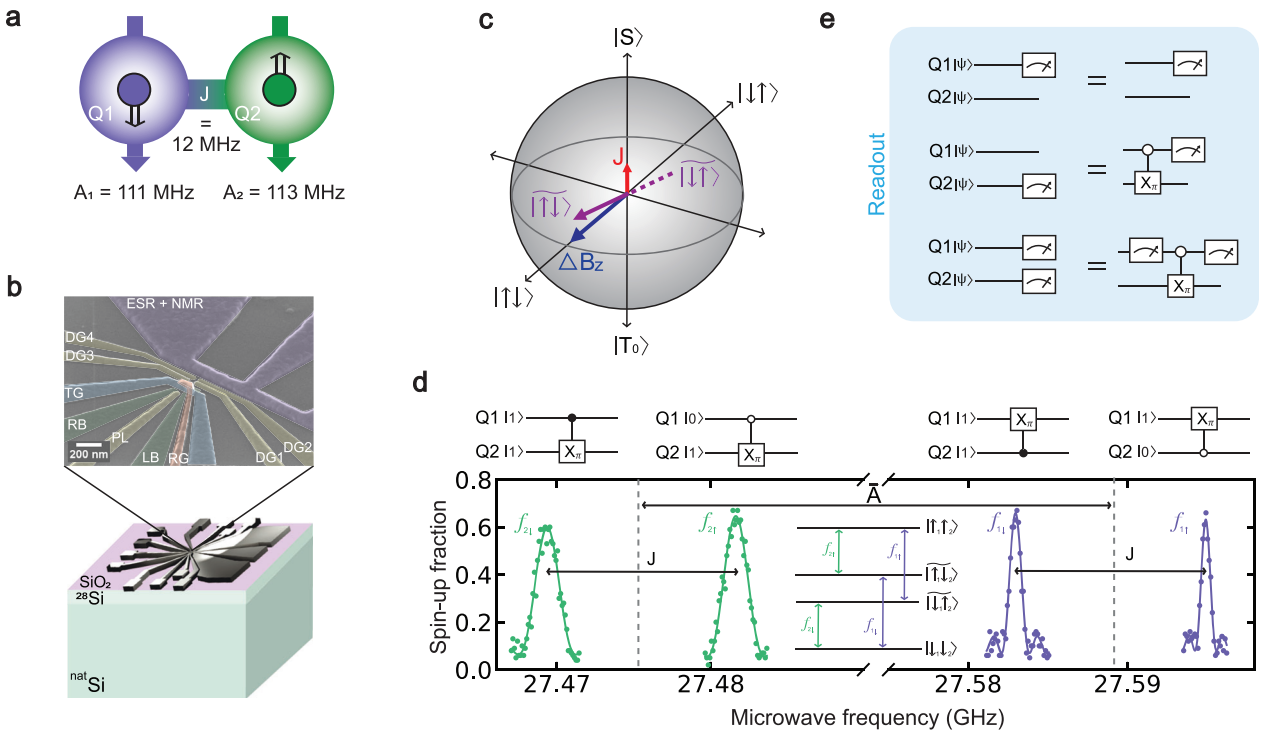

Fig. 1 | Two-qubit phosphorus device operation. a Schematic of the system consisting of two phosphorus donors, each with their own single, bound electron, denoted as Q1 and Q2. Setting the nuclei in an anti-parallel configuration results in an effective ΔB_z between the two electrons, which is given by the average hyperfine, $\bar{A}$, between the two donors. **b** Device layout showing the silicon substrate upon which Al gates are fabricated for device control and readout. The top of the figure shows an enlarged, false-coloured SEM image of the Al gate layout. **c** Bloch sphere denoting the hybridised states brought about by the ratio of the energy detuning ΔB_z with the exchange coupling J, which constitute the eigenstates of the system in the weak J regime. **d** ESR spectrum showing the resonant frequencies used to control Q1 (purple) and Q2 (green). These resonance frequencies are present when the nuclei are in an anti-parallel configuration of $|\Uparrow_1\Downarrow_2\rangle$. A resonant π pulse on any of these resonant frequencies represents a two-qubit CROT or zCROT gate, as shown in the circuit diagrams above each resonance. **e** Quantum circuits denoting the readout process for Q1 and Q2. Q1 is read out via spin-dependent tunnelling to a SET reservoir, while Q2 is instead read out indirectly via Q1 using quantum logic (see Supplementary Note 2).

where μ_B is the Bohr magneton, h is Planck's constant, $g_{1,2} \approx 1.9985$ the Landé g-factors of each electron spin, $g\mu_B/h \approx 27.97$ GHz/T and $\gamma_n \approx 17.23$ MHz/T is the ^{31}P nuclear gyromagnetic ratio.

We use aluminium gate electrodes, patterned on the surface of the silicon chip via electron-beam lithography, to control the electrostatic environment of the donors for donor initialisation and readout[29,33]. A broadband antenna delivers oscillating microwave or radio frequency (RF) magnetic fields to control the spin of the electrons and nuclei using electron spin resonance (ESR) or nuclear magnetic resonance (NMR), respectively (Fig. 1b). The donors are introduced in the silicon substrate using the industry-standard method of ion implantation. The device used here was fabricated in the same batch and with the same implantation parameters as the ones described in ref. 21. Among the 25 electrically functional devices we fabricated in that batch, three exhibited $J \approx 10$–30 MHz, and a fourth contained very tightly spaced donors, which were used to demonstrate nuclear two-qubit gates[14]. From the modelling of the implantation parameters[21] and the dependence of J on donor spacing[18], it is likely that many more devices may have contained exchange-coupled donor pairs with J in the desired range, but such pairs may not have been suitably located with respect to the single-electron transistor (SET) readout device.

The Q1 electron is read out and initialised directly via the standard method of energy-dependent tunnelling to a nearby SET island[30,34]. This readout also automatically initialises Q1 in the $|\downarrow\rangle$ ground state. To initialise Q2, we first prepare Q1 in the $|\downarrow\rangle$ state, before transferring the spin state from Q1 to Q2 using a process similar in nature to the well established electron-nuclear double resonance (ENDOR) technique[35] (see Supplementary Note 3, for details).

The Q2 electron readout involves using Q1 as ancilla in a repetitive, approximately quantum nondemolition (QND) scheme (see Supplementary Note 4)[31,32]. This is possible thanks to the electrons' long spin relaxation time ($T_1 \approx 1.4$ s), and the fact that $J \ll A$ renders the exchange interaction almost of Ising type, approximately fulfilling the QND condition[36]. The QND readout is performed by loading a $|\downarrow\rangle$ Q1 electron from the reservoir, rotating Q1 conditional on the state of Q2, reading out Q1, and repeating the cycle 11 times. The resulting readout contrast is greatly enhanced, from a bare 0.48 to 0.76. Secondly, the Q2 electron never leaves the donor, causing the neighbouring ^{29}Si nuclei to 'freeze'[37]. The sparse ^{29}Si nuclei surrounding the donor constitute a major source of decoherence and frequency jumps. Even in our isotopically enriched material, the 800 ppm residual ^{29}Si results in a few nuclei significantly coupled to the donor electron. Fluctuations in their orientation, caused by their internal dipole-dipole coupling, cause electron spin decoherence and discrete frequency jumps. However, such fluctuations are almost entirely suppressed while the electron is bound to the donor since the very different hyperfine couplings at each lattice site prevent energy-conserving dipolar flip-flops between the ^{29}Si nuclei.

In a similar fashion to the readout of electron Q2, the donor nuclei are read out indirectly via the Q1 electron. In order to read out the state of the nucleus of either donor 1 or 2, Q1 is initialised in the $|\downarrow\rangle$ state and then rotated conditional on the state of the nucleus, before being read out. As with electron Q2, the nuclei can hence be read out using QND readout, resulting in high nuclear readout fidelities, exceeding 99%[33]. The nuclei are initialised using an ENDOR technique[35] (see Supplementary Note 3).

Effect of weak exchange on qubit coherence

We investigated the effect of the exchange interaction on the coherence of the electrons by performing Ramsey and Hahn echo experiments on electron Q2, both with donor 1 in the neutral and ionised state. Donor 1 was ionised by tuning the device gate voltages such that electron Q1 is able to tunnel from the donor to the SET island. With the removal of Q1, the exchange coupling is no longer present in the system. The T_2^* and T_2^{Hahn} times of Q2 did not change within the error bars for the fits (shown in Fig. 2) with the removal of the exchange coupling, indicating that the noise in the exchange interaction is not a dominant source of decoherence of the qubits. This finding is consistent with results obtained in lithographic quantum dots operated in the regime $J < \Delta E_z$. In such devices, it was found that fluctuations in J were an insignificant source of dephasing compared to other noise sources[23,24]. Conversely, experiments conducted in the $J > \Delta E_z$ regime typically show a deterioration of spin coherence upon increasing J[5]. Our observation thus confirms the benefit of using the weak exchange regime for entangling operations.

Exchange-based two-qubit gates

Two-qubit controlled rotation (CROT) gates are naturally obtained by preparing the two donor nuclear spins in an anti-parallel configuration, i.e., either $|\Downarrow\Uparrow\rangle$ or $|\Uparrow\Downarrow\rangle$ (Fig. 1a). In doing so, the two-electron spins are frequency-detuned by the average hyperfine coupling $\overline{A} = \frac{(A_1+A_2)}{2}$. This can be thought of as the switchable, digital version of the detuning caused by a gradient in Overhauser field ΔB_z in double quantum dots[3], i.e., $\Delta B_z = \pm\overline{A}$ (Fig. 1c).

The two-electron spin eigenstates of the system are shown in Table 1, where $\tan(2\theta) = J/\overline{A}$. In the present device, $J \approx 12$ MHz $\ll \overline{A} \approx 112$ MHz results in $\cos(\theta) = 0.9986$, so that the eigenstates are almost (but not exactly) the tensor products of the individual spins' basis states $\{|\downarrow\rangle, |\uparrow\rangle\}$.

For each anti-parallel nuclear state, there exist two ESR frequencies for electron Q1, which are separated by J and represent the following transitions: $|\downarrow\downarrow\rangle \leftrightarrow |\uparrow\underset{\sim}{\downarrow}\rangle$ and $|\downarrow\underset{\sim}{\uparrow}\rangle \leftrightarrow |\uparrow\uparrow\rangle$. Similarly, for electron Q2, two ESR resonances exist for each anti-parallel nuclear state, which represent the transitions: $|\downarrow\downarrow\rangle \leftrightarrow |\downarrow\underset{\sim}{\uparrow}\rangle$ and $|\uparrow\underset{\sim}{\downarrow}\rangle \leftrightarrow |\uparrow\uparrow\rangle$. A π pulse applied at any of these resonance frequencies represents the inversion of one electron, conditional on the state of the other electron. By defining $|\downarrow\rangle$ as the computational $|1\rangle$ state and $|\uparrow\rangle$ as the computational $|0\rangle$ state, a CROT gate is therefore implemented by applying a π pulse at the resonance to flip the target electron conditional on the control electron being in the $|1\rangle$ state, while a zCROT operation is implemented by applying a π pulse at the resonance to flip the target electron conditional on the control electron being in the $|0\rangle$ state. For the entirety of this work we therefore set the nuclei into the anti-parallel spin configuration $|\Uparrow_1\Downarrow_2\rangle$. The native CROT gates obtained in this way are equivalent to the resonant gates in double quantum dots with fixed exchange coupling[22,24], where the detuning between Q1 and Q2 is created either by a g-factor difference or by a magnetic field gradient. This resonant CROT only requires J to be larger than the ESR linewidth (~100 kHz for donor electrons in ^{28}Si) and smaller than the detuning (here given by $\overline{A} \sim 100$ MHz), making this gate robust against donor placement uncertainties.

Characterising gate performance

In order to fully characterise this J-coupled system, we performed one-qubit GST in two separate ways. First, we characterised the one-qubit, unconditional gates. Since the native gates in this J-coupled system are two-qubit CROT operations, an unconditional one-qubit gate is implemented by two sequential CROT gates, in order to rotate one electron unconditionally on the state of the other electron[24]. We performed GST on a gate set consisting of a $\pi/2$ rotation about the X axis of the Bloch sphere ($X_{\frac{\pi}{2}}$), a $\pi/2$ rotation about the Y axis ($Y_{\frac{\pi}{2}}$), and an idle operation (I). This gate set was characterised for both Q1 and Q2, with the idle electron initialised in either the $|\downarrow\rangle$, $\frac{1}{\sqrt{2}}(|\downarrow\rangle + |\uparrow\rangle)$ or $|\uparrow\rangle$ state. Figure 3 shows the estimated error budgets for these unconditional operations, as extracted from the estimated error rates. Notwithstanding the longer gate times compared to the native conditional operations, fidelities of both $X_{\frac{\pi}{2}}$ and $Y_{\frac{\pi}{2}}$ exceeded 99.00 ± 0.29%. Here and elsewhere, error bars indicate 2σ confidence intervals.

https://doi.org/10.1038/s41467-024-52795-4

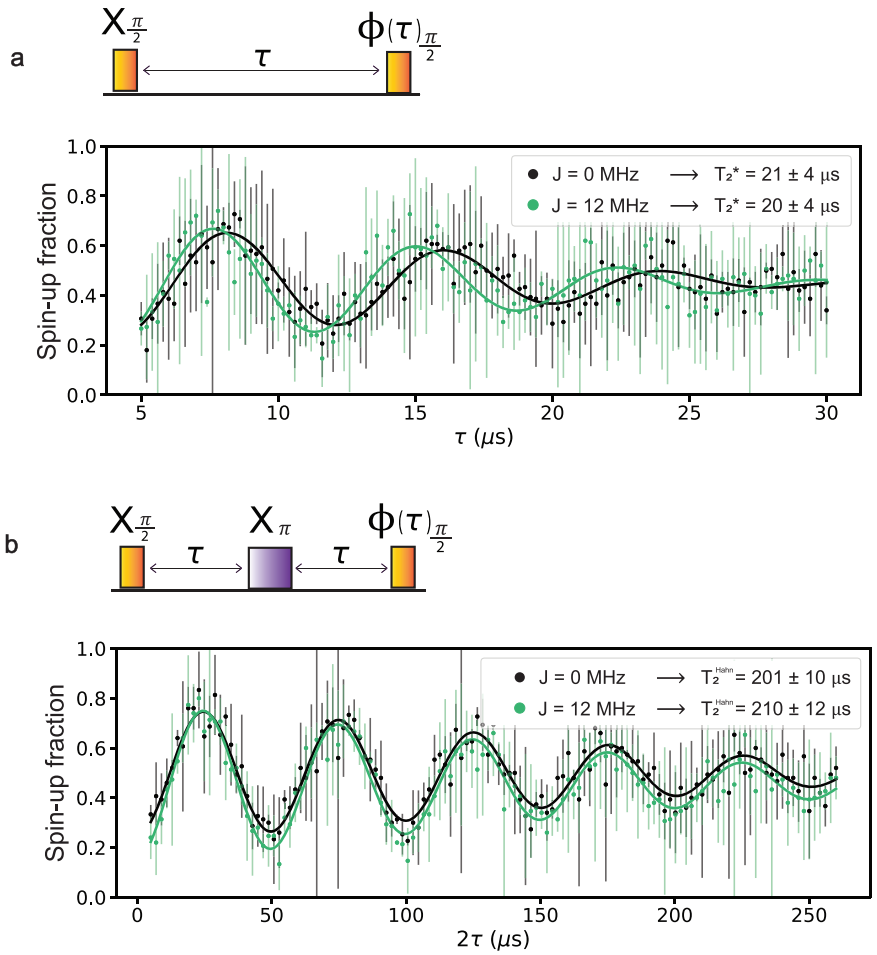

Fig. 2 | Effect of weak exchange on electron coherence time. a Electron spin dephasing measurements by Ramsey experiment performed on Q2 with (green) and without (black) the presence of an exchange interaction J with Q1. The $J = 0$ regime was created by ionising nucleus 1, i.e., by completely removing the Q1 electron. **b** Hahn echo experiment performed on Q2 with and without the presence of the exchange coupling. The oscillations are artificially introduced by a wait time-dependent phase shift added to the final $\frac{\pi}{2}$ pulse. In all cases, the exchange coupling produces no detectable reduction in spin coherence times. In both the Ramsey and the Hahn echo experiments, each individual experiment [preparation, pulses, wait time, electron readout] was repeated 50 times. The entire Ramsey and Hahn echo experiments were then repeated multiple times, with the mean of the first three repetitions of the experiment plotted. The error bars represent 2σ of these three repetitions.

We then performed one-qubit GST on the conditional one-qubit gates, in all four contexts: acting on Q1 and Q2, conditional on the control electron being initialised in either the $|\downarrow\rangle$ or $|\uparrow\rangle$ state. As with the case of the unconditional gates, we analysed a gate set consisting of $X_{\frac{\pi}{2}}$, $Y_{\frac{\pi}{2}}$. Each gate was iteratively calibrated using the one-qubit GST analysis results. The value of coherent over- or under-rotation error extracted by GST was used to update the rotation angle of the electron in the next round of experiments until the coherent errors were smaller than their own error bars. Figure 4 shows the estimated error budgets for each of these four native conditional operations. The $X_{\frac{\pi}{2}}$ and $Y_{\frac{\pi}{2}}$ gates both have fidelity exceeding 99.63 ± 0.07% for all four of the native conditional rotations.

Table 1 | Two-qubit electron spin states

|Q1Q2⟩	Eigenbasis	S_z basis
|11⟩	$\|\downarrow\downarrow\rangle$	$\|\downarrow\downarrow\rangle$
|10⟩	$\widetilde{\|\downarrow\uparrow\rangle}$	$\cos(\theta)\|\downarrow\uparrow\rangle + \sin(\theta)\|\uparrow\downarrow\rangle$
|01⟩	$\widetilde{\|\uparrow\downarrow\rangle}$	$\cos(\theta)\|\uparrow\downarrow\rangle - \sin(\theta)\|\downarrow\uparrow\rangle$
|00⟩	$\|\uparrow\uparrow\rangle$	$\|\uparrow\uparrow\rangle$

Next, we performed full two-qubit GST on a gate set consisting of conditional $X_{\frac{\pi}{2}}$ and $Y_{\frac{\pi}{2}}$ rotations for each of the four configurations of the native conditional two-qubit operation (Fig. 5), together with a global idle giving 9 gates in total. The analysis of the two-qubit GST results tells a more complicated story, revealing error mechanisms that were otherwise invisible when operating the device as an effective one-qubit system as above. The error budget in the two-qubit case is dominated by three main sources. For the two-qubit conditional rotation gates, there are systematic coherent errors that correspond to relational axis-misalignment errors between pairs of $X_{\frac{\pi}{2}}$ and $Y_{\frac{\pi}{2}}$ gates acting on different control and target qubits. Additionally, the two-qubit conditional rotation gates induce a significant amount of dephasing on the control qubit. For the idle gate, on the other hand, the error is predominantly dephasing.

To help understand the underlying physical error channels, we separate out coherent errors, mostly attributable to the control system and potentially correctable through calibration, from stochastic errors, which typically arise from device physics. We perform this partition using the generator fidelity introduced in[14], and find that the two-qubit conditional rotation gates have incoherent contributions to their infidelities ranging from 6.91% to 21.88%, with an average of 12.54 ± 6.40% (see Supplementary Note 9 for details).

https://doi.org/10.1038/s41467-024-52795-4

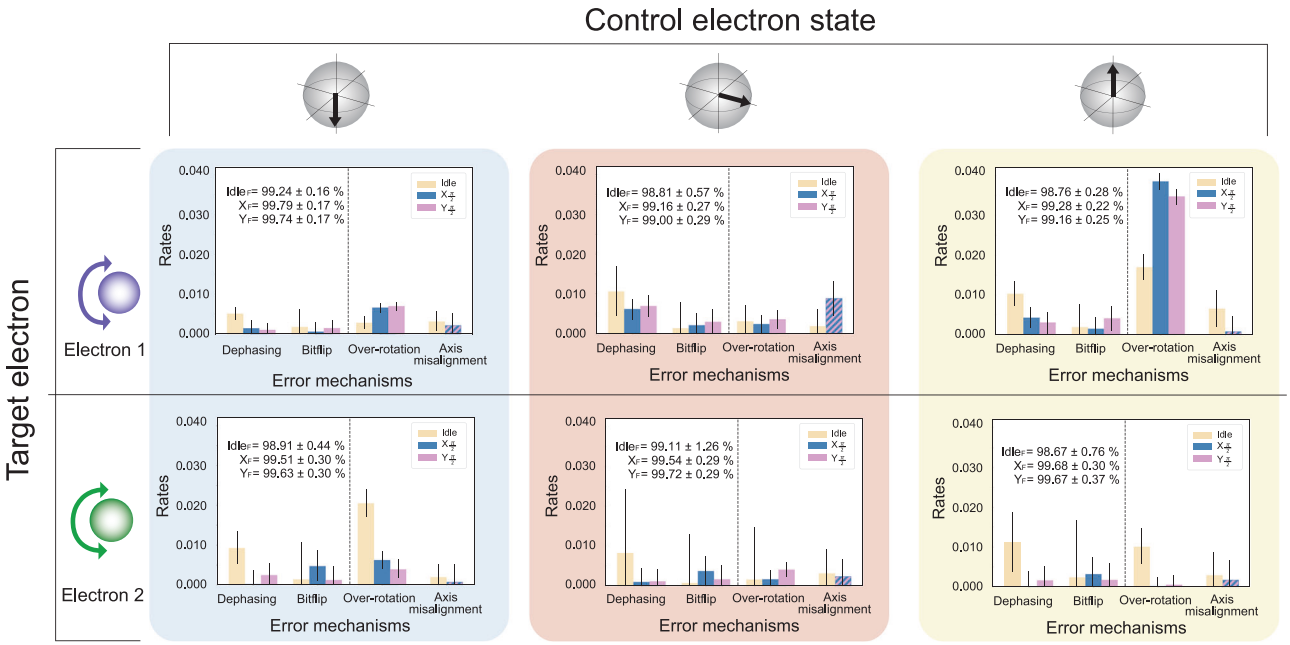

Fig. 3 | Unconditional one-qubit GST. Characterisation of the unconditional one-qubit gates, using one-qubit GST. The unconditional gates were implemented by applying two sequential $\frac{\pi}{2}$ rotations to the target electron, one conditional on the control electron being in the spin $|\downarrow\rangle$ state and one conditional on the control electron being in the $|\uparrow\rangle$ state, in order to rotate one electron unconditional on the state of the other electron. To test the effectiveness of this unconditional gate, we performed three separate GST experiments on each electron, with the other electron initialised in either the $|\downarrow\rangle$ state, a superposition state of $\frac{1}{\sqrt{2}}(|\downarrow\rangle+|\uparrow\rangle)$ or the $|\uparrow\rangle$ state. The diagrams to the left of the rows indicate which electron is acting as the target electron in each GST experiment, while the Bloch sphere schematics above each of the columns denotes the state of the corresponding control electron throughout each GST experiment. The error rates can be broken down into the two stochastic error sources: dephasing and bitflip errors (to the left of the black dashed line), and two coherent error sources: over-rotation and axis-misalignment (to the right of the black dashed line). The axis-misalignment of the $X_{\frac{\pi}{2}}$ and $Y_{\frac{\pi}{2}}$ gates, on the other hand, represents the error in the relative angle between the X and Y rotation axes of the qubit and hence is represented by a single striped column, to indicate that this error is associated with both the $X_{\frac{\pi}{2}}$ and $Y_{\frac{\pi}{2}}$ gates. For a full description of how the error rates for each physical error mechanism were calculated see Supplementary Note 8 (sub-note 3). The fidelities estimated for each gate, X_F, Y_F, and Idle_F, are quoted in the inset of each plot. For a full breakdown of the error rates extracted from GST for the unconditional one-qubit operations, see Supplementary Note 8 (sub-note 2). The error bars represent confidence intervals of 2σ.

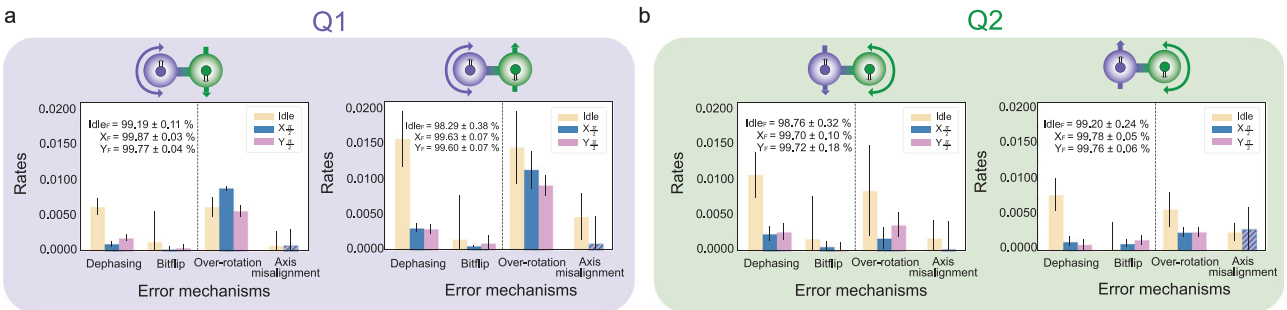

Fig. 4 | Conditional one-qubit GST on both electrons. a Gate characterisation of the native, conditional gates performed on electron Q1, estimated using one-qubit GST. The schematics above each plot depict the state in which electron Q2 was initialised and upon which each gate on Q1 was conditioned, for the two separate GST experiments. **b** Error rates for the native, conditional gates performed on electron Q2, estimated using one-qubit GST. Stochastic error mechanisms are shown to the left of the black dashed line on each plot, while coherent error mechanisms are shown to the right of the black dashed line. For more information regarding how each physical error mechanism was extracted, see Supplementary Note 8 (sub-note 3). The fidelities estimated for each gate are quoted in the inset of each plot. For a full breakdown of the error rates for the conditional one-qubit operations, see Supplementary Note 8 (sub-note 1). The error bars represent confidence intervals of 2σ.

The much lower gate fidelities obtained from two-qubit GST compared to one-qubit GST are a remarkable observation, given that all operations in a fixed-J system are natively two-qubit conditional gates. This suggests that device-specific error mechanisms may have a more severe effect than previously recognised. We conjecture, for example, that much of the observed increase in dephasing on the control qubit can be attributed to jumps in the resonance frequency of the target qubit, induced by changes in the orientation of a few weakly coupled ^{29}Si nuclei, as discussed in the sections above. These frequency jumps are small (~10 kHz) in absolute terms, but their impact may be magnified by the geometric phase ϕ_c induced on the control qubit upon performing a rotation of the target qubit. Since ϕ_c is half the solid angle traversed by the target qubit on the Bloch sphere[14], its value can depend very sensitively on the detuning $\Delta\nu_t$ between the instantaneous resonance frequency of the target qubit and the frequency of the microwave driving field. Even a small shift $\Delta\nu_t \ll 2\nu_{\text{Rabi}}$,

https://doi.org/10.1038/s41467-024-52795-4

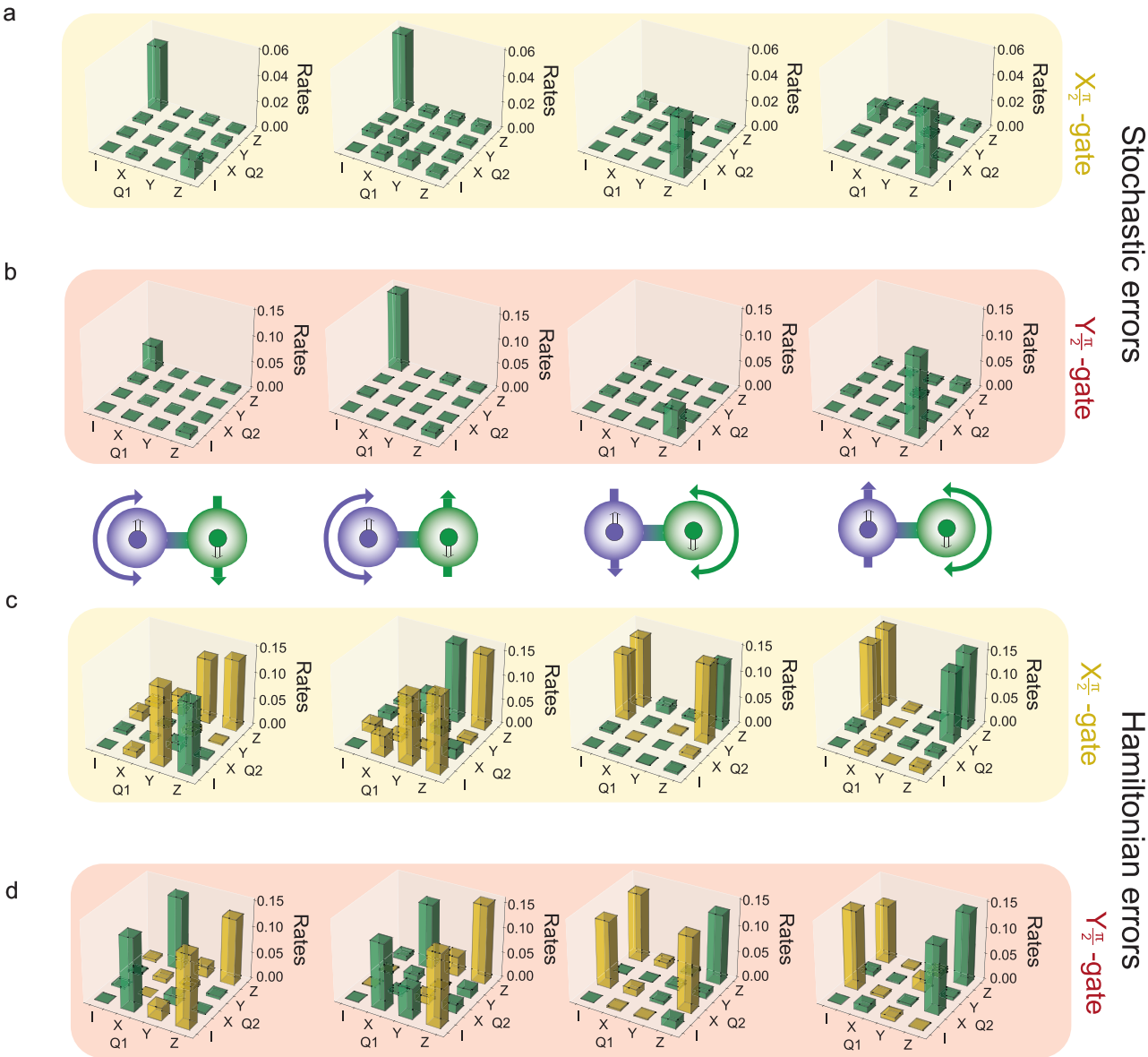

Fig. 5 | Two-qubit GST on the electrons. Stochastic and Hamiltonian error rates were estimated using two-qubit GST for both the $X_{\frac{\pi}{2}}$ (**a**, **c**) and $Y_{\frac{\pi}{2}}$ (**b**, **d**) gates. From left to right in **a**, **c** (**b**, **d**) these $X_{\frac{\pi}{2}}$($Y_{\frac{\pi}{2}}$) rotations were performed on Q1, conditional on Q2 being in the $|\downarrow\rangle$ state, Q1 conditional on Q2 being in the $|\uparrow\rangle$ state, Q2 conditional on Q1 being in the $|\downarrow\rangle$ state and Q2 conditional on Q1 being in the $|\uparrow\rangle$ state. These eight gates were all tested in the same two-qubit GST experiment. The full error rates estimated from this two-qubit GST experiment are shown in Supplementary Note 9.

where ν_{Rabi} is the Rabi frequency of the target electron, can alter the path traversed by the target qubit in the Bloch sphere of its rotating frame, and cause a stochastic error on the phase of the control qubit. Frequency jumps caused by more strongly coupled ^{29}Si nuclei, with $\Delta\nu_t > 100$ kHz, can be mitigated by checking (e.g., with a quick Ramsey measurement) and re-calibrating the resonance frequency. This strategy becomes increasingly difficult if $\Delta\nu_t$ approaches the intrinsic linewidth of the target qubit, proportional to $1/T_2^*$ (≈ 20 kHz). In these cases, pulse engineering could be utilised to design a drive that is more robust against these small shifts in the resonance frequency. Additional work is currently underway validating this conjecture and exploring other possible decoherence mechanisms that could be partially responsible for the observed dephasing rates.

Electron spin Bell state tomography

We demonstrated the entangling nature of the two-qubit CROT operations by creating and tomographing electron Bell states. We created a two-electron Bell state by initialising the spins in the state $|\mathrm{Q1Q2}\rangle = |\downarrow\downarrow\rangle$, performing an X_2^π gate on Q1, and then an entangling CROT operation on Q2. The fidelity of the resulting state was benchmarked using phase reversal tomography[38–41], whereby the pulses used to create the Bell state are applied in reverse, but with a progressively increasing phase (Fig. 6a). Accordingly, the ability to reverse the electrons back to their initial state oscillates according to the phase of the reversal pulses. This results in the spin-up proportion $P_{\uparrow 1}(\theta)$ of the Q1 electron oscillating as a function of reversal phase θ, where $P_{\uparrow 1}(0) = 0$ indicates that the electrons have been perfectly reversed to their initial state. The amplitude and phase of these oscillations allow for the reconstruction of the off-diagonal corner elements of the two-qubit density matrix, ρ_{14}, ρ_{41}. In order to obtain the diagonal corner elements, ρ_{11}, ρ_{44}, we directly measured the Bell state populations in the Z-basis immediately following the state's preparation. By choosing to prepare the $\Phi^+ = \frac{1}{\sqrt{2}}(|\downarrow\downarrow\rangle + |\uparrow\uparrow\rangle)$ Bell state, which only has non-zero elements in each of the four corners of the density matrix, the

https://doi.org/10.1038/s41467-024-52795-4

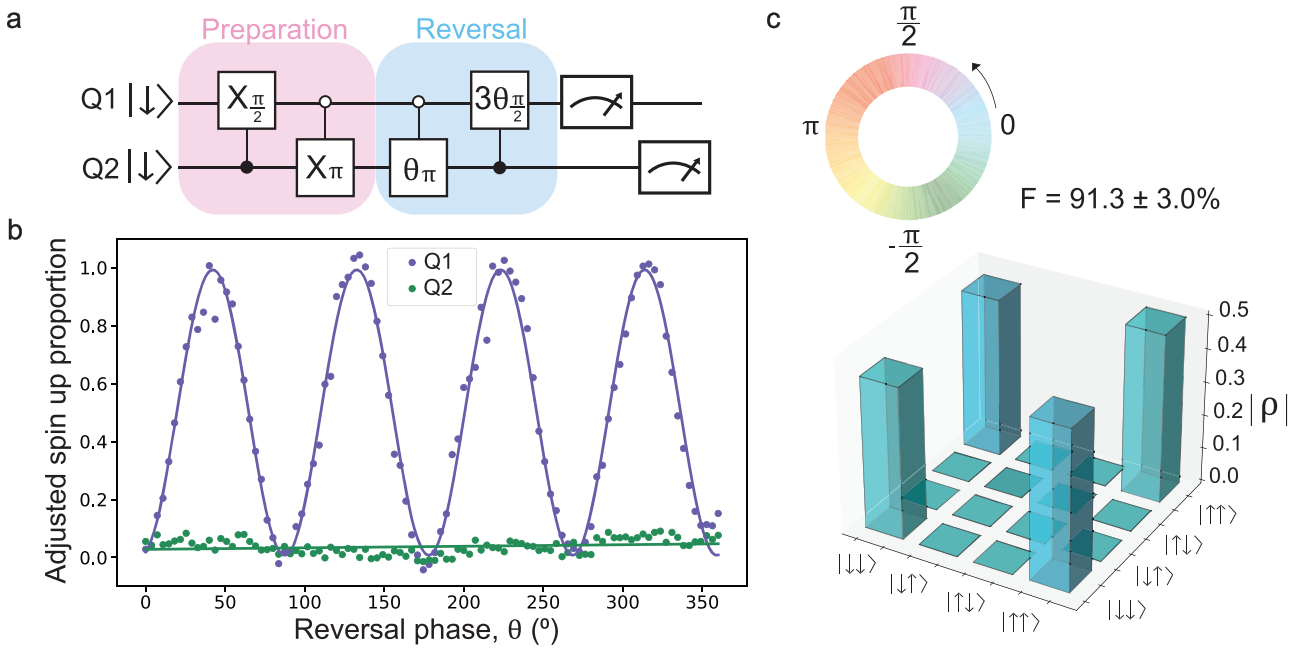

Fig. 6 | Phase reversal tomography of a two-electron Bell state. a Circuit diagram associated with the preparation of the $\Phi^+ = \frac{1}{\sqrt{2}}(|\downarrow\downarrow\rangle + |\uparrow\uparrow\rangle)$ Bell state. **b** Oscillation in the spin-up proportion of electron Q1 and Q2 as a function of the phase of the reversal pulses, with the amplitude of the oscillations adjusted to account for state preparation and measurement (SPAM) error. **c** Reconstructed density matrix of the Φ^+ state using phase reversal tomography. The magnitude of the density matrix elements are represented by the height of the respective bars, while the phase of each element is denoted by the associated colour on the colour wheel. From this density matrix, a Bell state fidelity of $F = 91.3 \pm 3.0\%$ was extracted.

fidelity of this Bell state can be ascertained using these four matrix elements. Using this method, we obtained a Bell state fidelity of 91.3 ± 3.0%, with state preparation and measurement (SPAM) error removed, and 72.5 ± 2.0% without SPAM removal (Supplementary Note 10). An optimisation algorithm was used to find the closest physical density matrix to the measured density matrix, ρ. A concurrence value of 0.87 ± 0.05 was obtained from the SPAM-removed density matrix (Supplementary Note 10 and 11), indicating a high degree of entanglement between Q1 and Q2.

Discussion

We demonstrated an entangling two-qubit gate between two exchange-coupled electrons bound to ion-implanted ^{31}P donors in silicon, by exploiting the hyperfine interaction to provide a natural source of detuning ΔB_z between the two qubits. This method works for any value of J between the ESR linewidth (~100 kHz) and the hyperfine coupling (~100 MHz), making it robust against the precise placement of the donors. Furthermore, we showed that the small value of J results in the qubit coherence being unaffected by the coupling.

Gate set tomography experiments showed that both conditional and unconditional one-qubit gate fidelities consistently surpass 99%. However, the full two-qubit GST showed an increased error rate, likely caused by the coupling to nearby ^{29}Si nuclei (Supplementary Note 12). This observation motivates the adoption of ^{28}Si isotopic enrichment far beyond the 800 ppm residual ^{29}Si used in this experiment[37,42]. Promising results, with residual ^{29}Si concentrations of 2.4 ± 0.7 ppm have been recently obtained using focused ion beam implantation of ^{28}Si[43].

The value of exchange coupling $J \approx 12$ MHz in the present device corresponds to an expected inter-donor distance in the range of 15–22 nm[18]. This distance is comparable to the smallest feature sizes of ultra-scaled semiconductor devices that use industrial CMOS fabrication[44]. Therefore, two-qubit logic gates based on weak exchange provide a plausible pathway to integrate and scale up single-donor quantum devices.

In the medium term, scaling up beyond two qubits is likely to involve coupling donors to quantum dots at the Si/SiO_2 interface, and then using chains of quantum dots[45] or 'jellybean' elongated dots[46] to reach beyond the ~20 nm range. Small logical qubit structures could be built this way[47], or extended to full-scale surface code architectures[48]. The donor nuclear spin can act as a 'digital detuning' between the donor and dot electrons[49], or be used directly as a long-lived, high-fidelity qubit where the electrons act as entanglement mediators[14]. The possibility of coupling to interface quantum dots is a unique feature of the MOS-compatible, ion-implanted donor fabrication route. The demonstration of entanglement between the electrons of two ion-implanted donors provided here constitutes the key stepping stone to unlocking hybrid, scalable spin-based quantum computer architectures in silicon.

Methods

Sample fabrication

For the device fabrication, an isotopically enriched epilayer of ^{28}Si, with a residual ^{29}Si concentration of 730 ppm, is grown atop a silicon wafer. A 200 nm thick SiO_2 field oxide is grown via a wet oxidation process, while in the active region of the device, a high-quality 8 nm thermal oxide layer is grown in dry conditions. In order to implant the devices with donor atoms, a 90 nm x 100 nm implantation window is defined using electron-beam lithography (EBL). Donor atoms are then implanted into this window at an acceleration voltage of 10 kV and implantation dose of 1.4×10^{12} cm^{-2}. Using SRIM simulations, we have estimated that at this implantation energy, the implantation profile of the donors should exist in a range of approximately 10 nm from the oxide interface. A rapid thermal anneal for 5 s at 1000 °C is carried out following implantation in order to repair the damage inflicted to the

lattice during implantation and to activate the donors. Aluminium gates are then fabricated on the surface of the chip in three separate EBL steps, with each step being followed by a thermal deposition of aluminium, followed by exposure to pure, low-pressure oxygen to form an Al_2O_3 layer between each gate layer. A forming gas anneal (95% N_2, 5% H_2) for 15 min at 400 °C is then performed in order to passivate any interface traps.

Experimental setup

The device is glued to a copper enclosure, through a cut out in a custom printed circuit board (PCB), that contains both microwave and low frequency lines. The device is then aluminium wire bonded to the PCB and bolted to a permanent magnet assembly, which provides a strong, static magnetic field. The permanent magnet assembly is mounted onto the mixing chamber plate of a Bluefors BF-LD400 cryogen-free dilution refrigerator, which cools the device to a base temperature of approximately 20 mK.

DC voltages are sourced by 9 Stanford Research systems (SRS) SIM 928 DC sources, hosted in two SIM 900 mainframes. The DC lines consist of a constantan loom, which is low pass filtered with a 20 Hz cutoff at the mixing chamber stage. Three of the donor gates also have an AC input to allow for fast dynamic tuning of these gate voltages. These RF signals are provided by a Keysight M3300A arbitrary waveform generator (AWG), which is bandwidth limited to 200 MHz, and passed into the AC inputs of AC/DC combiners for these gates, to allow an RF modulation to be added on top of the static DC voltage. The RF lines are made from a flexible copper-nickel (Cu-Ni) coaxial line. These lines are graphite coated to reduce triboelectric noise and filtered to a cutoff frequency of 145 MHz at the mixing chamber plate.

A Keysight M3201A module hosts a field-programmable gate array (FPGA), on which we have built an in-house direct digital synthesis (DDS) system. The DDS provides RF input signals to the I and Q inputs of a Keysight E8267D PSG vector microwave source, to allow for single and dual-sideband modulation of a microwave tone produced by the vector source, for control of the electron spin. Additionally, the DDS provides the RF signal for control of the nuclear spin through NMR. The NMR signal is attenuated by 10 dB at room temperature, to protect the antenna from any unexpected spikes in NMR amplitude, before being combined with the microwave output of the vector source using a DPX1721 diplexer, allowing both NMR and ESR signals to travel down the same line to the device's antenna. This line consists of a semi-rigid, silver-plated Cu-Ni coaxial line. The line then passes through an inner/outer DC block at room temperature, to prevent possible voltage offsets from creating a DC current through the thin short circuit termination of the microwave antenna. Additionally, this line is attenuated by a further 10 dB, with an attenuator positioned at the 4K stage of the dilution refrigerator.

The SET current returning from the drain is passed through a Basel SP983c transimpedence amplifier, which converts the current into a voltage with a gain of 10^7 V/A and frequency bandwidth of 100 kHz. The voltage signal is then passed into a SIM911 bipolar junction transistor (BJT) amplifier, which is housed in the same SIM900 mainframe as the DC sources and provides an additional gain of 10^2. This amplifier also has the function of breaking the ground between the fridge and the measurement setup. As the BJT amplifier can add additional noise to the current signal, the signal is passed through a further passive low pass filter, with a cutoff at 100 kHz. The signal then enters the digitiser channel of the Keysight M3300A, with a sample rate of 100 megasamples-per-second.

Data availability

The source data and analysis scripts generated in this study can be found in the following repository https://doi.org/10.5061/dryad.w3r2280zm.

References

1. Burkard, G., Ladd, T. D., Pan, A., Nichol, J. M. & Petta, J. R. Semiconductor spin qubits. *Rev. Mod. Phys.* **95**, 025003 (2023).
2. Loss, D. & DiVincenzo, D. P. Quantum computation with quantum dots. *Phys. Rev. A* **57**, 120 (1998).
3. Petta, J. R. et al. Coherent manipulation of coupled electron spins in semiconductor quantum dots. *Science* **309**, 2180 (2005).
4. Maune, B. M. et al. Coherent singlet-triplet oscillations in a silicon-based double quantum dot. *Nature* **481**, 344 (2012).
5. Veldhorst, M. et al. A two-qubit logic gate in silicon. *Nature* **526**, 410 (2015).
6. Eenink, H. et al. Tunable coupling and isolation of single electrons in silicon metal-oxide-semiconductor quantum dots. *Nano Lett.* **19**, 8653 (2019).
7. Nurizzo, M.et al. Controlled quantum dot array segmentation via highly tunable interdot tunnel coupling. *Appl. Phys. Lett.* **121,** 084001 (2022).
8. Reed, M. et al. Reduced sensitivity to charge noise in semiconductor spin qubits via symmetric operation. *Phys. Rev. Lett.* **116**, 110402 (2016).
9. Martins, F. et al. Noise suppression using symmetric exchange gates in spin qubits. *Phys. Rev. Lett.* **116**, 116801 (2016).
10. Morello, A., Pla, J. J., Bertet, P. & Jamieson, D. N. Donor spins in silicon for quantum technologies. *Adv. Quantum Technol.* **3**, 2000005 (2020).
11. Kane, B. E. A silicon-based nuclear spin quantum computer. *Nature* **393**, 133 (1998).
12. Muhonen, J. T. et al. Storing quantum information for 30 seconds in a nanoelectronic device. *Nat. Nanotechnol.* **9**, 986 (2014).
13. Muhonen, J. T. et al. Quantifying the quantum gate fidelity of single-atom spin qubits in silicon by randomized benchmarking. *J. Phys. Condens. Matter* **27**, 154205 (2015).
14. Madzik, M. T. et al. Precision tomography of a three-qubit donor quantum processor in silicon. *Nature* **601**, 348 (2022).
15. Dehollain, J. P. et al. Optimization of a solid-state electron spin qubit using gate set tomography. *N. J. Phys.* **18**, 103018 (2016).
16. Koiller, B., Hu, X. & Sarma, S. D. Exchange in silicon-based quantum computer architecture. *Phys. Rev. Lett.* **88**, 027903 (2001).
17. Voisin, B. et al. Valley interference and spin exchange at the atomic scale in silicon. *Nat. Commun.* **11**, 6124 (2020).
18. Joecker, B., Baczewski, A. D., Gamble, J. K., Saraiva, A. & Andrea, M. Full configuration interaction simulations of exchange-coupled donors in silicon using multi-valley effective mass theory. *N. J. Phys.* **23**, 073007 (2021).
19. He, Y. et al. A two-qubit gate between phosphorus donor electrons in silicon. *Nature* **571**, 371 (2019).
20. Kalra, R., Laucht, A., Hill, C. D. & Morello, A. Robust two-qubit gates for donors in silicon controlled by hyperfine interactions. *Phys. Rev. X* **4**, 021044 (2014).
21. Madzik, M. T. et al. Conditional quantum operation of two exchange-coupled single-donor spin qubits in a mos-compatible silicon device. *Nat. Commun.* **12**, 181 (2021).
22. Zajac, D. M. et al. Resonantly driven CNOT gate for electron spins. *Science* **359**, 439 (2018).
23. Noiri, A. et al. Fast universal quantum gate above the fault-tolerance threshold in silicon. *Nature* **601**, 338 (2022).
24. Huang, W. et al. Fidelity benchmarks for two-qubit gates in silicon. *Nature* **569**, 532 (2019).
25. Jakob, A. M. et al. Deterministic shallow dopant implantation in silicon with detection confidence upper-bound to 99.85% by ion–solid interactions. *Adv. Mater.* **34**, 2103235 (2022).

26. Holmes, D. et al. Improved placement precision of donor spin qubits in silicon using molecule ion implantation. *Adv. Quantum Technol.* **7**, 2300316 (2024).
27. Jakob, A. M. et al. Scalable atomic arrays for spin-based quantum computers in silicon. *Adv. Mater.* 240006 (2023).
28. Pillarisetty, R. et al. Qubit device integration using advanced semiconductor manufacturing process technology. in *2018 IEEE International Electron Devices Meeting (IEDM)*. 6–3 (IEEE, 2018)
29. Pla, J. J. et al. A single-atom electron spin qubit in silicon. *Nature* **489**, 541 (2012).
30. Morello, A. et al. Single-shot readout of an electron spin in silicon. *Nature* **467**, 687 (2010).
31. Nakajima, T. et al. Quantum non-demolition measurement of an electron spin qubit. *Nat. Nanotechnol.* **14**, 555 (2019).
32. Xue, X. et al. Repetitive quantum nondemolition measurement and soft decoding of a silicon spin qubit. *Phys. Rev. X* **10**, 021006 (2020).
33. Pla, J. J. et al. High-fidelity readout and control of a nuclear spin qubit in silicon. *Nature* **496**, 334 (2013).
34. Elzerman, J. et al. Single-shot read-out of an individual electron spin in a quantum dot. *Nature* **430**, 431 (2004).
35. Tyryshkin, A. M., Morton, J. J., Ardavan, A. & Lyon, S. Davies electron-nuclear double resonance revisited: enhanced sensitivity and nuclear spin relaxation. *J. Chem. Phys.* **124**, 234508 (2006).
36. Joecker, B., Stemp, H. G., Fernández de Fuentes, I., Johnson, M. A. & Morello, A. Error channels in quantum nondemolition measurements on spin systems. *Phys. Rev. B* **109**, 085302 (2024).
37. Madzik, M. T. et al. Controllable freezing of the nuclear spin bath in a single-atom spin qubit. *Sci. Adv.* **6**, eaba3442 (2020).
38. Mehring, M., Mende, J. & Scherer, W. Entanglement between an electron and a nuclear spin 1/2. *Phys. Rev. Lett.* **90**, 153001 (2003).
39. Sackett, C. A. et al. Experimental entanglement of four particles. *Nature* **404**, 256 (2000).
40. Wei, K. X. et al. Verifying multipartite entangled Greenberger-Horne-Zeilinger states via multiple quantum coherences. *Phys. Rev. A* **101**, 032343 (2020).
41. Dehollain, J. P. et al. Bell's inequality violation with spins in silicon. *Nat. Nanotechnol.* **11**, 242 (2016).
42. Witzel, W. M., Carroll, M. S., Morello, A., Cywiński, Ł. & Sarma, S. D. Electron spin decoherence in isotope-enriched silicon. *Phys. Rev. Lett.* **105**, 187602 (2010).
43. Acharya, R. et al. Highly ^{28}Si enriched silicon by localised focused ion beam implantation. *Commun. Mater.* **5**, 57 (2024).
44. Cao, W. et al. The future transistors. *Nature* **620**, 501 (2023).
45. Chan, K. W. et al. Exchange coupling in a linear chain of three quantum-dot spin qubits in silicon. *Nano Lett.* **21**, 1517 (2021).
46. Wang, Z. et al. Jellybean quantum dots in silicon for qubit coupling and on-chip quantum chemistry. *Adv. Mater.* **35**, 2208557 (2023).
47. Jones, C. et al. Logical qubit in a linear array of semiconductor quantum dots. *Phys. Rev. X* **8**, 021058 (2018).
48. Pica, G., Lovett, B. W., Bhatt, R. N., Schenkel, T. & Lyon, S. A. Surface code architecture for donors and dots in silicon with imprecise and nonuniform qubit couplings. *Phys. Rev. B* **93**, 035306 (2016).
49. Harvey-Collard, P. et al. Coherent coupling between a quantum dot and a donor in silicon. *Nat. Commun.* **8**, 1029 (2017).

Acknowledgements

This research was funded by the Australian Research Council Centre of Excellence for Quantum Computation and Communication Technology (CE170100012) and the US Army Research Office (Contracts no. W911NF-17-1-0200 and W911NF-23-1-0113). We acknowledge the facilities, and the scientific and technical assistance provided by the UNSW node of the Australian National Fabrication Facility (ANFF), and the Heavy Ion Accelerators (HIA) nodes at the University of Melbourne and the Australian National University. ANFF and HIA are supported by the Australian Government through the National Collaborative Research Infrastructure Strategy (NCRIS) programme. H.G.S., M.R.v.B., A.V. acknowledge support from the Sydney Quantum Academy. C.I.O, K.M.R, K.C.Y, and R.J.B-K acknowledge funding in part by the U.S. Department of Energy, Office of Science, Office of Advanced Scientific Computing Research Quantum Testbed Pathfinder Programme. The views and conclusions contained in this document are those of the authors and should not be interpreted as representing the official policies, either expressed or implied, of the Army Research Office or the U.S. Government. The U.S. Government is authorised to reproduce and distribute reprints for Government purposes, notwithstanding any copyright notation herein. Sandia National Laboratories is a multimission laboratory managed and operated by National Technology & Engineering Solutions of Sandia, LLC, a wholly-owned subsidiary of Honeywell International Inc., for the U.S. Department of Energy's National Nuclear Security Administration under contract DE-NA0003525. This paper describes objective technical results and analysis. Any subjective views or opinions that might be expressed in the paper do not necessarily represent the views of the U.S. Department of Energy or the United States Government.

Author contributions

H.G.S., S.A., A.L., and A.M. conceived and designed the experiments. H.G.S., S.A., M.R.vB., A.V., M.A.I.J., A.J.A.H., H.R.F. performed and analysed the measurements. M.T.M. and F.E.H. fabricated the device, with A.S.D.'s supervision, on materials supplied by K.M.I., A.M.J., B.C.J., and D.N.J. designed and performed the ion implantation. C.I.O., K.M.R., K.Y. and R.B.-K. contributed to the GST analysis. R.Y.S. and C.H.Y. contributed to the data analysis. H.G.S. and A.M. wrote the manuscript with input from all coauthors. A.M. supervised the project.

Competing interests

A.M. and A.L. are coauthors on a patent that describes the quantum logic operations used in this work (AU2013302299B2, US10878331B2, EP2883194B1). A.S.D. is the CEO and a director of Diraq Pty Ltd. C.H.Y., A.L., F.E.H., and A.S.D. declare equity interest in Diraq Pty Ltd. The remaining authors declare no competing interests.

Additional information

Supplementary information The online version contains supplementary material available at https://doi.org/10.1038/s41467-024-52795-4.

Correspondence and requests for materials should be addressed to Andrea Morello.

Peer review information *Nature Communications thanks* Dohun Kim, Luke Pendo, and the other anonymous reviewers for their contribution to the peer review of this work. A peer review file is available.